Supplementary Information of:

Direct observation of anomalous CO_2 dispersion in multi-scale porous media

Qihui Wu[a, b], Yulin Zhang[a, b], Yibo Yang[a, b], Jun Yao[a, b], Yongfei Yang[a, b], Hai Sun[a, b], Lei Zhang[a, b], Junjie Zhong[a, b, *]

[a] *National Key Laboratory of Deep Oil and Gas, China University of Petroleum (East China), Qingdao 266580, P.R. China*

[b] *Research Center of Multiphase Flow in Porous Media, School of Petroleum Engineering, China University of Petroleum (East China), Qingdao, China, 266580*

*Corresponding author: Prof. Junjie Zhong, E-mail address: zhongjunjie@upc.edu.cn

Number of pages: 29

Number of texts: 4

Number of figures: 17

Number of tables: 2

Contents

Text S1 Micromodels design and fabrication

1 Core properties extraction

To reconstruct the 3D structure of the core's microscopic pores, X-ray micro-CT (SkysCan2211) scanning were conducted with a resolution of 2.5 μm. Cubic cores measuring 5cm × 5cm × 5cm were extracted from core with permeabilities of 10.2 mD. A total of 1800 high-resolution slice images were selected for micromodel design. The raw images were processed using median filtering and thresholding segmentation (Liu et al., 2024). The maximal ball algorithm was used to segment pores and identify throats, while a simplified pore network model was employed to calculate the pore-throat coordination number and permeability of the cores and micromodels (Blunt and Dong, 2009). The hydraulic pore diameter distribution and reference porosity of the cores were determined using Mercury Intrusion Porosimetry (MIP) tests (AutoPore Iv 9510).

2 Pore and throat design

Pores were designed through image binarization and threshold segmentation. We first superimposed all binarized CT images to generate a pore density image, then applied a threshold δ to define pixels with grayscale values below the specified threshold as pores (assigned value 1), with remaining regions designated as "matrix" (assigned value 0).

Throats were designed by identifying connectivity regions between pores and performing watershed segmentation. The watershed algorithm was applied to the "matrix" regions after threshold segmentation to extract the medial axes (K. et al., 1998; Song et al., 2024). Each pixel along the medial axis was subsequently dilated. The dilation width was proportional to the shortest Euclidean distance to the geometric center of the matrix. And then, a connectivity disruption was applied to simulate hydraulic blockage resulting from cementation and compaction processes (Li et al., 2019; Makhloufi et al., 2013). Digital rock analysis revealed a proportional

relationship between pore volume and coordination number (Figure S2). Accordingly, we calculated the distance (d) between each throat and the geometric center of its nearest connected pore. A critical threshold θ was established, wherein throats with $d_t < \theta$ were considered "cemented or compacted".

3 Fracture design

Fractures were designed using a stochastic growth method to simulate stress-induced dynamic fracture propagation in a simplified method (Huang et al., 2022; Lecampion et al., 2018; Li et al., 2016). With a constant fracture dip angle (set parallel to the injection direction in this study), the fracture centerline propagated at random angles α (constrained between 90° and -90°) for random lengths. Starting from the fracture center, each section expanded perpendicularly to angle α by width d, which gradually decreased from the fracture center towards the tips. Schematic diagrams of the generated fractures are shown in Figure 1 (c) and Figure S1 (d).

4 Micromodel fabrication

The micromodels were fabricated on silicon wafers with multiple cycles of photolithography and deep reactive ion etching, followed by anodic bonding to a glass wafer (Ratanpara et al., 2025; Ren et al., 2013). The entire fabrication process was conducted in a cleanroom environment to prevent particulate contamination of the microchannels.

Text S2 Procedure of displacement experiments

Two syringe pumps were used to control the injection and back pressures, respectively (Figure 2). The water and CO_2 were contained in two high-pressure fluid containers and pre-pressurized to 9 MPa. A high-pressure fluid container at the outlet was used to collect the effluent and to prevent unnecessary fluctuations of back pressure. The temperature was maintained by a circulator bath. The testing water was prepared by dissolving 0.1 wt% bromocresol green and 0.02 wt% methyl orange in deionized water, with the pH adjusted to 7 ± 0.5 using NaOH (Cooper, 1941; King and Kester, 1989). Here, bromocresol green and methyl orange were used to track CO_2-induced acidification of water during CO_2 dispersion. The testing CO_2 consisted of pure CO_2 (> 99%). All chemical reagents were purchased from Sinopharm Chemical Reagent Co., Ltd.

In a typical experimental run, the micromodel was cleaned, dried, and evacuated firstly. The water phase was then injected (over 100 pore volumes) via the left syringe pump to achieve complete water saturation. Subsequently, the water-saturated micromodel was extracted and positioned. All tubes were drained and purged with CO_2. After reinstalling the water-saturated micromodel, valves 1, 4, and 6 were then opened to pressurize the tubes and micromodel to 9 MPa with CO_2, while the syringe pump 1 maintained stable pressure. With valve 4 open, simultaneous pressurization at both ends of the chip prevented internal fluid movement. Finally, the left syringe pump was switched to constant flow rate to inject CO_2, while the right syringe pump remained in constant pressure (9 MPa). Three injection flow rates were tested in this study: 1, 5, and 23 μL/min. Real-time observation of localized regions within the micromodel was conducted using a microscope (Nikon NIU) and a CMOS camera (PCO Panda, 1824×1216 pixels).

Text S3 Total carbon concentration calculation

The ion equilibrium, hydrolysis equilibrium constant of CO_2 (K_H), ionization equilibrium of H_2CO_3 (K_{a1} and K_{a2}), and water self-ionization constant (K_w) in solution are given by Eqs. S1–S5.

$$c_{(HCO_3^-)} + 2 * c_{(CO_3^{2-})} + c_{(OH^-)} = c_{(H^+)} \tag{S1}$$

$$K_H = \frac{c_{(H_2CO_3)}}{c_{(CO_2)}} \tag{S2}$$

$$K_{a1} = \frac{c_{(H^+)} * c_{(HCO_3^-)}}{c_{(H_2CO_3)}} \tag{S3}$$

$$K_{a2} = \frac{c_{(H^+)} * c_{(CO_3^{2-})}}{c_{(HCO_3^-)}} \tag{S4}$$

$$K_w = c_{(H^+)} * c_{(OH^-)} \tag{S5}$$

Here, we neglect the effects of trace amounts of dyes and the NaOH used for pH adjustment on the ion equilibrium. From Eq S1 to S5, the formula for calculating total carbon concentration based on pH is given by Eq S6 (Birgisson et al., 2025).

$$\begin{aligned} c_{tol} &= c_{(CO_2)} + c_{(H_2CO_3)} + c_{(HCO_3^-)} + c_{(CO_3^{2-})} \\ &= \frac{c_{(H_2CO_3)}}{K_H} + \frac{c_{(HCO_3^-)} * c_{(H^+)}}{K_{a1}} + c_{(HCO_3^-)} + c_{(CO_3^{2-})} \\ &= \frac{c_{(HCO_3^-)} c_{(H^+)}}{K_{a1} K_H} + \frac{c_{(HCO_3^-)} * c_{(H^+)}}{K_{a1}} + c_{(HCO_3^-)} + \frac{K_{a2} c_{(HCO_3^-)}}{c_{(H^+)}} \\ &= \frac{1}{1 + 2 * \frac{K_{a2}}{c_{(H^+)}}} * \left(c_{(H^+)} - \frac{K_w}{c_{(H^+)}} \right) * \left(\frac{c_{(H^+)}}{K_{a1} K_H} + \frac{c_{(H^+)}}{K_{a1}} + 1 + \frac{K_{a2}}{c_{(H^+)}} \right) \end{aligned} \tag{S6}$$

Here, ionization constant of water (K_w) is calculated using the density model (Eq S7)(Marshall and Franck, 1981), where a, b, c, d, e, f, g are fitting parameters adopted from Arcis et al. (Arcis et al., 2024; Arcis et al., 2020), T and ρ_w are the test temperature and the density of water under experimental conditions.

$$\log_{10} K_w = a + \frac{b}{T} + \frac{c}{T^2} + \frac{d}{T^3} + \left(e + \frac{f}{T} + \frac{g}{T^2} \right) \log_{10} \rho_w \tag{S7}$$

CO_2 hydration rate constant (K_H) is calculated using Eq S8(Soli and Byrne, 2002),

$$\log_{10} K_H = 22.66 - 7799 T^{-1} \tag{S8}$$

while the first (K_{a1}) and second (K_{a2}) dissociation constant of carbonic acid are calculated using Eqs S9 and S10 respectively (Plummer and Busenberg, 1982).

$$K_{a1} * K_H = -356.3094 - 0.06091964T + \frac{21834.37}{T} + 126.8339\log_{10}T - \frac{1684915}{T} \quad \text{(S9)}$$

$$K_{a2} * K_H = -107.8871 - 0.03252894T + \frac{5151.79}{T} + 38.92561\log_{10}T - \frac{563713.9}{T} \quad \text{(S10)}$$

Text S4 Correction fitting method for micromodel with fracture

Using the partially connected micromodel with fracture at 5 μL/min as an example (Figure 6 (c)), for Stage I, the CO_2 concentration in the aqueous phase increases from zero, allowing direct power-law fitting. But for Stage II and III, since the dispersion processes across stages are relatively independent, we first need to determine the initial dispersion time t_0 for each stage. As shown in Figure S5, we fitted the $\log\sigma^2$ vs. $\log t$ data for Stage II, where the fitted line intersects the $\log\sigma^2$ values at the initial and stable time points, marked as A and B respectively. The time coordinates of A and B (t_A and t_B) represent the initial and stable times for Stage II dispersion. Subsequently, we set t_A as the initial time and refitted the data between points A and B, obtaining $\alpha = 0.93$ for Stage II dispersion. The above processing was applied to both Stage II and Stage III $\log\sigma^2$ vs. $\log t$ data, as shown in Figure S6.

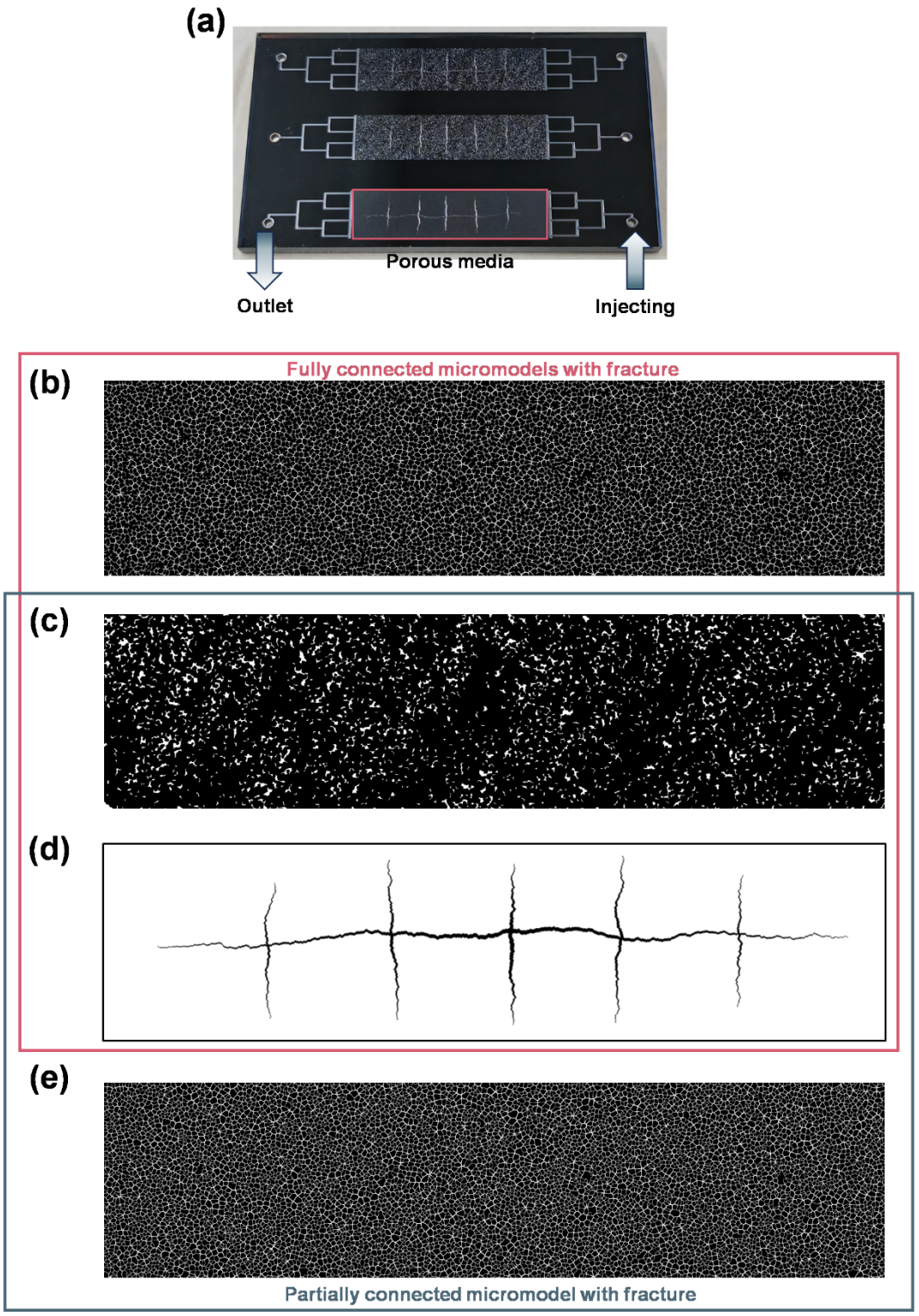

Figure S1. (a) Micromodel. (b)-(e) Complete design of first-scale pores for fully connected micromodel with fracture and partially connected micromodel with fracture, (b) throats of fully connected micromodel with fracture, (c) pores, (d) fracture, and (e) throats of partially connected micromodel with fracture.

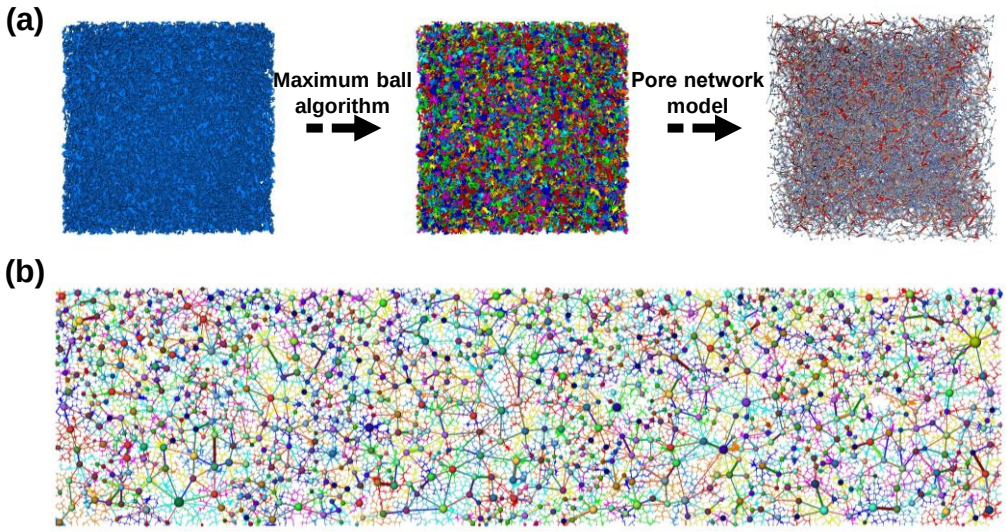

Figure S2. (a) Workflow for determining core properties using the pore network model. (b) Pore network model of the partially connected micromodel.

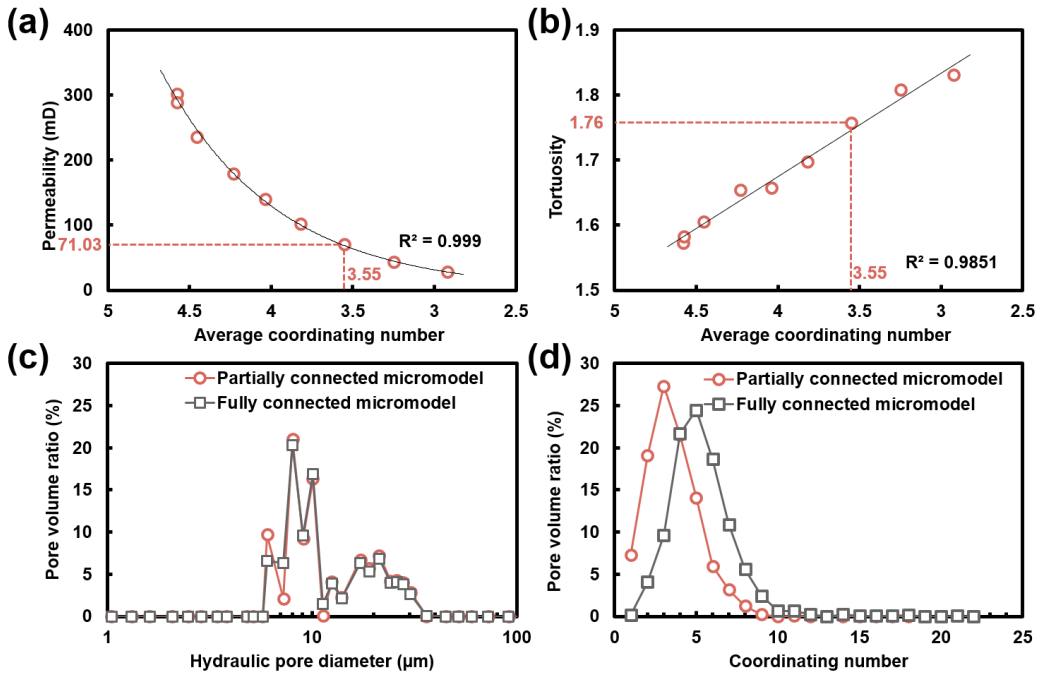

Figure S3 Permeability (a) and tortuosity (b) of micromodel with different coordination numbers. Hydraulic pore diameter distribution (c) and coordinating number distribution (d) of partially and fully connected micromodels.

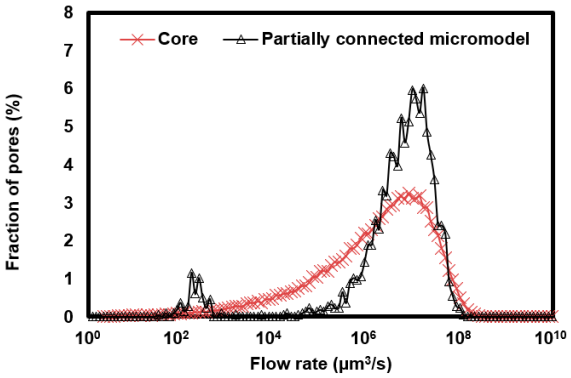

Figure S4 Probability density distributions of flow rates for core and partially connected micromodel.

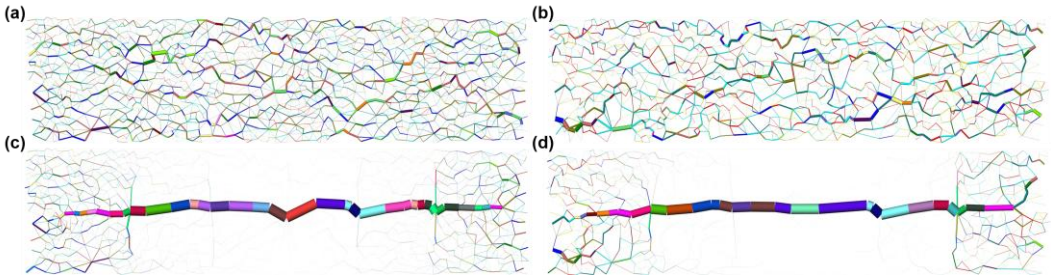

Figure S5 Flow rate distributions for fully connected micromodel (a), partially connected micromodel (b), fully connected micromodel with fracture (c) and partially connected micromodel with fracture (d), at an injection rate of 5 µL/min, with throat width scaled to the corresponding volumetric flux.

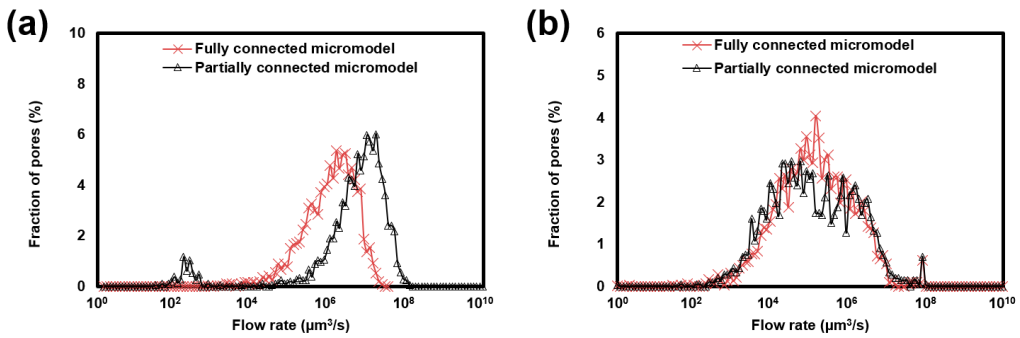

Figure S6 Probability density distributions of flow rates for fully and partially connected micromodel (a), and fully and partially connected micromodel with fracture (b).

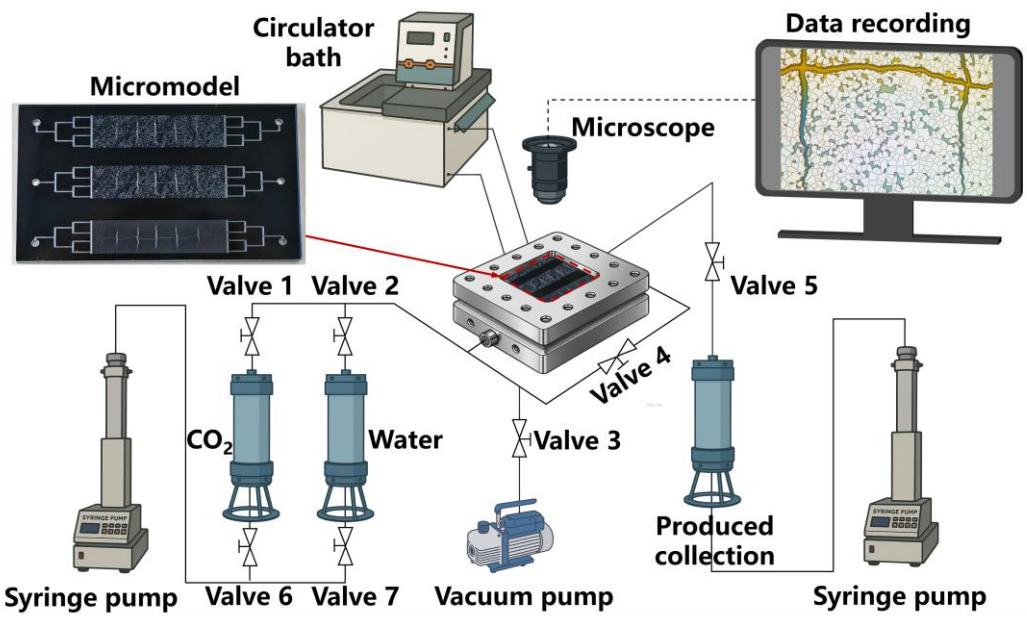

Figure S7 Experimental setup.

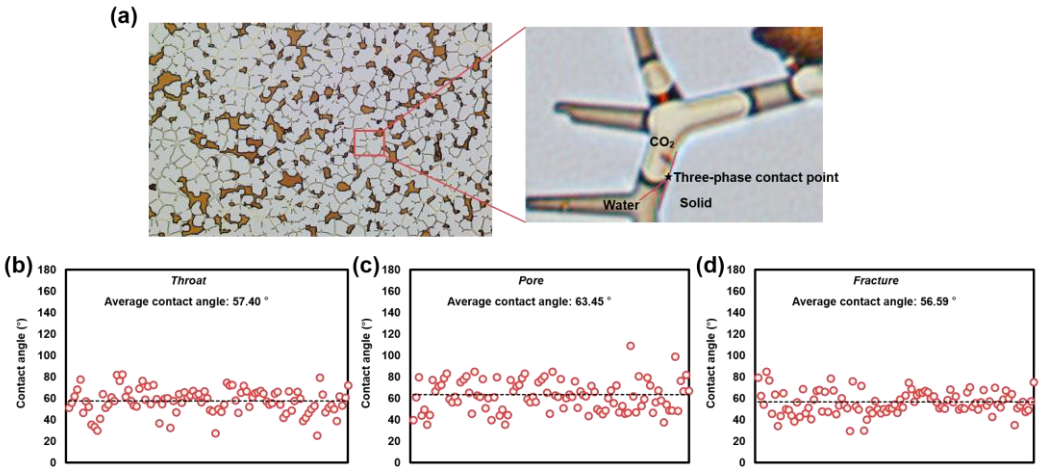

Figure S8 (a) In-situ measurement of contact angles. (b)-(d) Contact angles of throats (b), pores (c), and fractures (d).

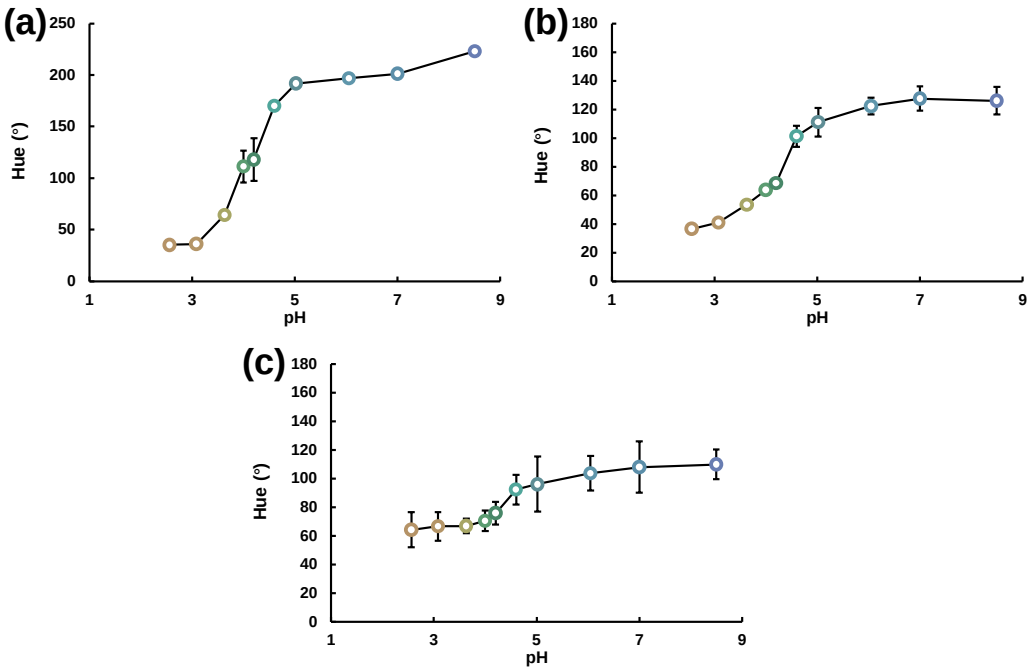

Figure S9. Calibration curve for (a) fracture (70 µm depth), (b) pores (22 µm depth), and (c) throats (8 µm depth).

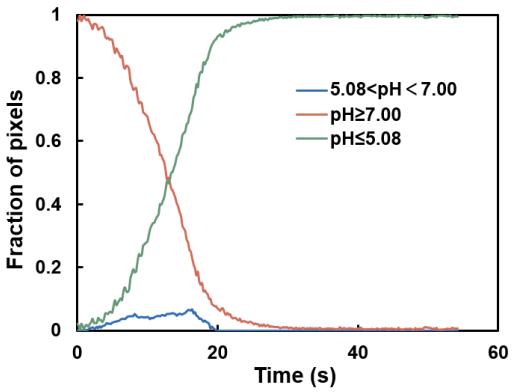

Figure S10 Proportion of image pixels falling within three pH intervals throughout the entire experiment for the partially connected micromodel at an injection rate of 5 µL/min.

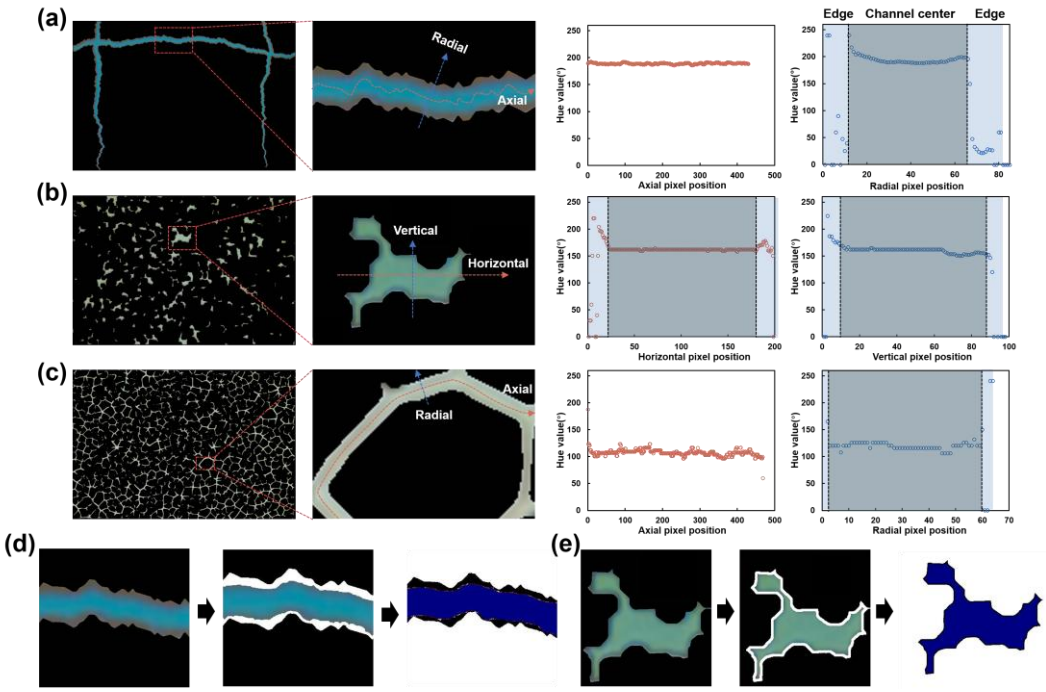

Figure S11 Assessment and mitigation of non-uniform etching effects on colorimetric pH measurements. (a - c) Local magnified images and hue value profiles of a representative fracture (a), pore (b), and throat (c). (d - e) Masking of non-uniformly etched edge regions for a fracture (d) and a pore (e).

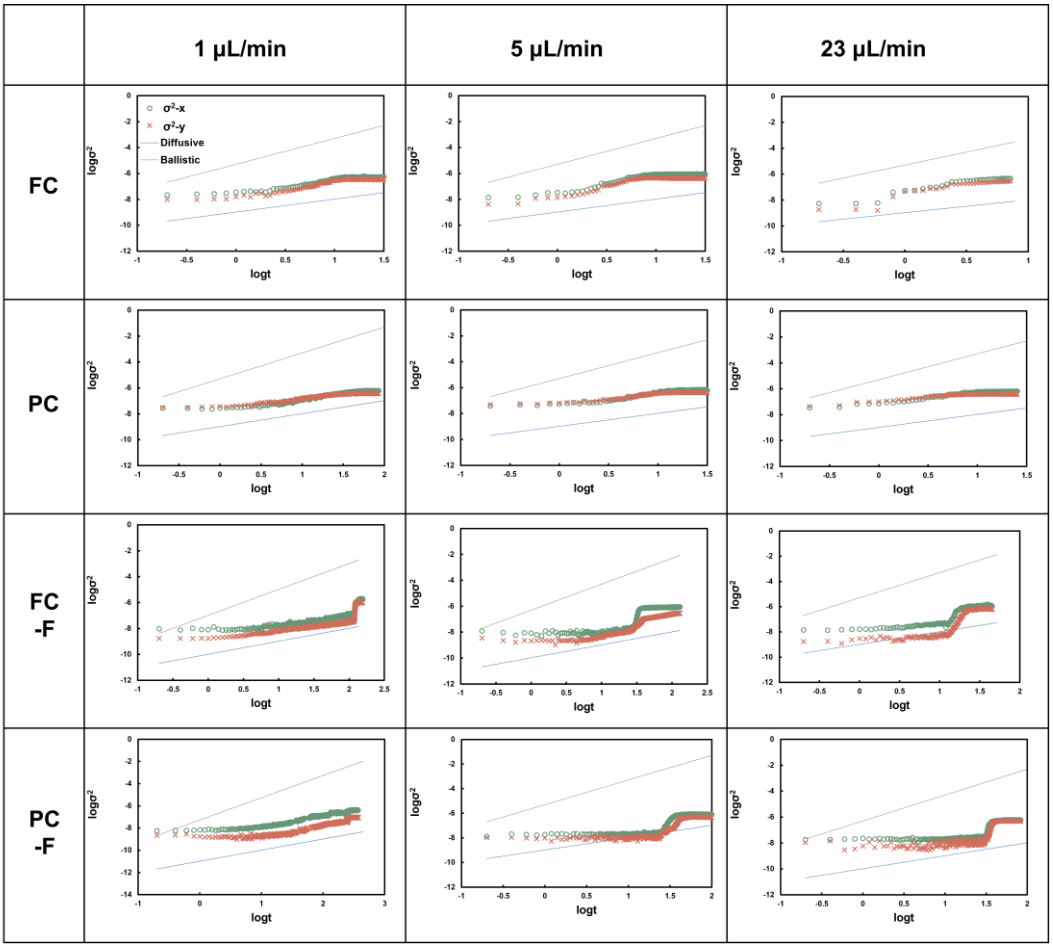

Figure S12. $\log \sigma^2$ vs. $\log t$ for experimental groups with different micromodels and injection rates.

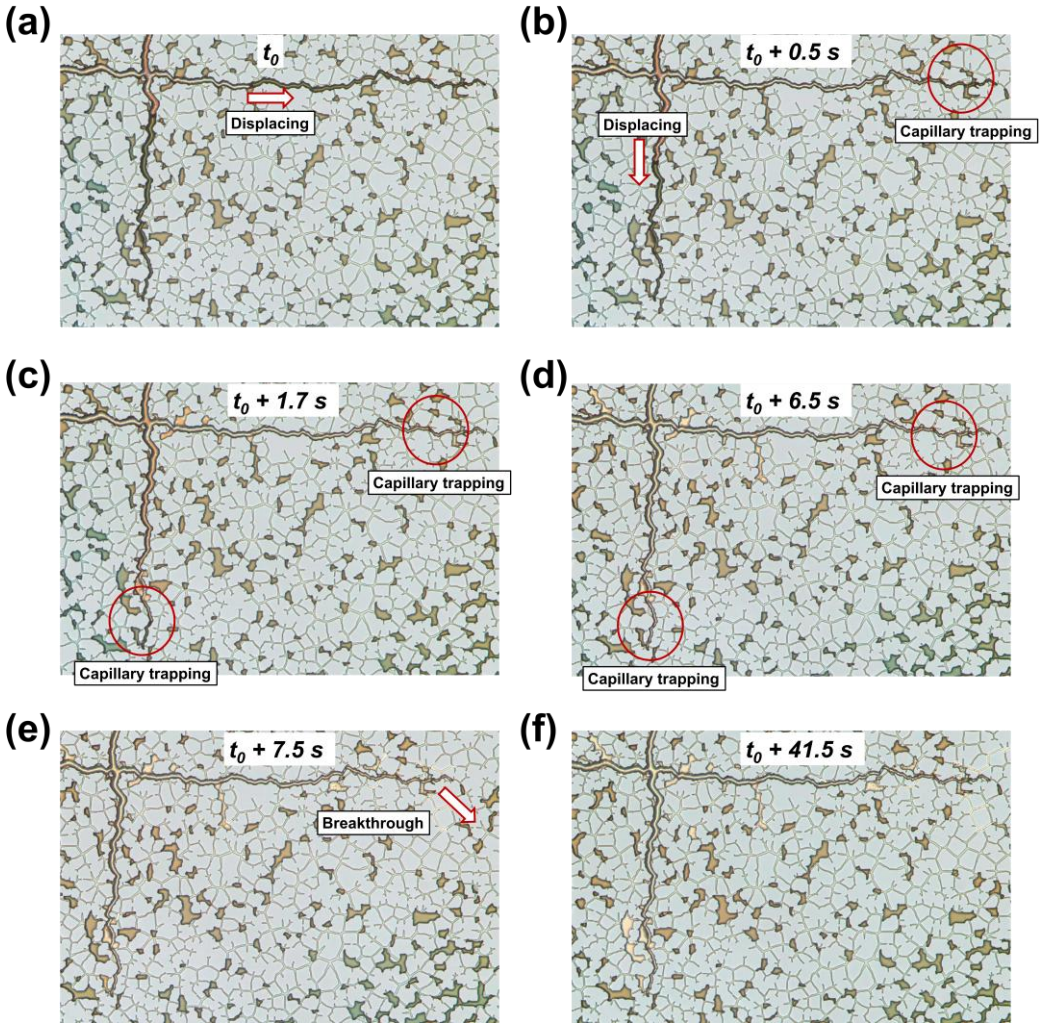

Figure S13. Capillary force induced fracture-matrix crossflow at the tail of fracture.

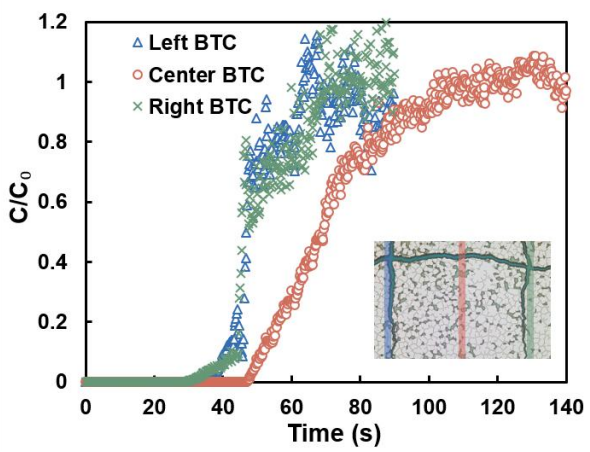

Figure S14 Breakthrough curves in the partially connected micromodel with fracture.

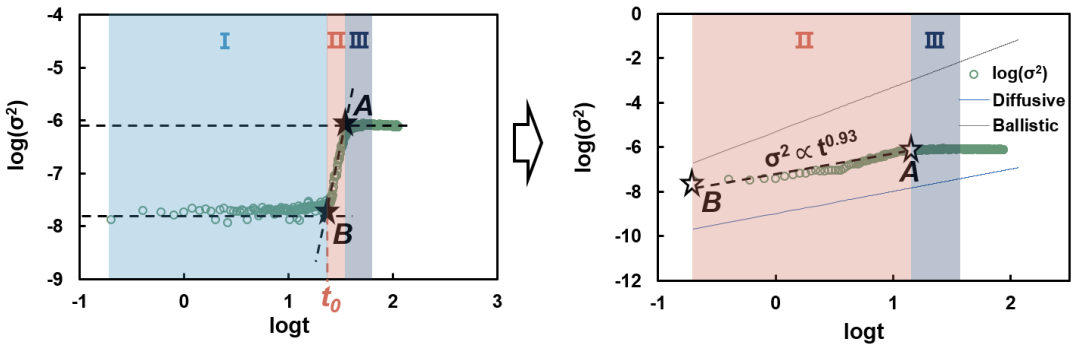

Figure S15. Schematic illustration of correction fitting method for Stage II and Stage III (using Stage II of partially connected micromodel with fracture as an example).

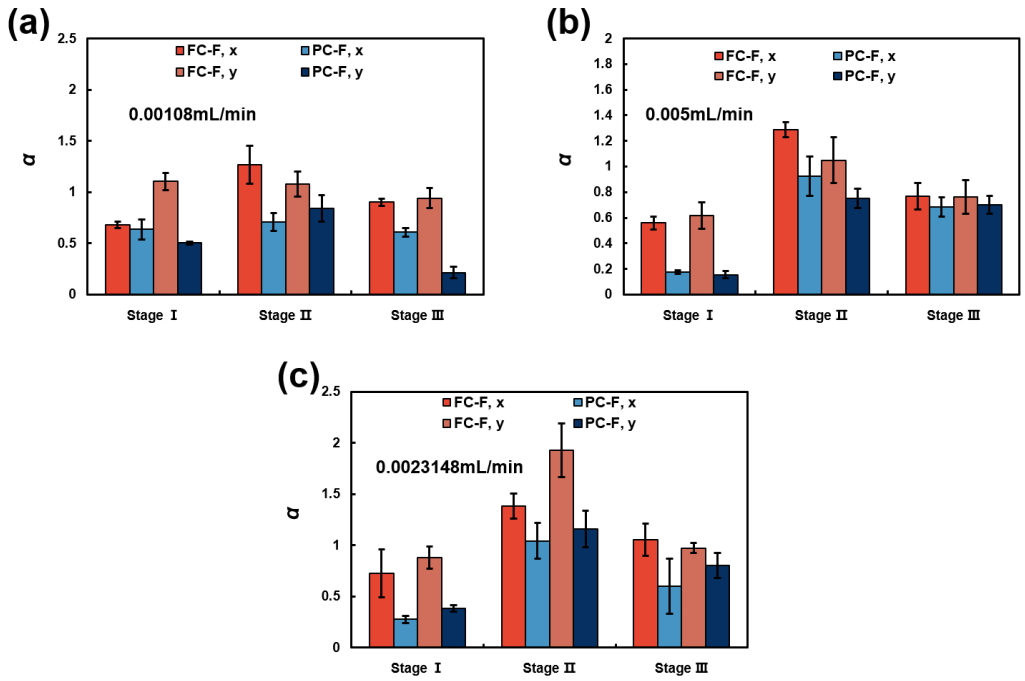

Figure S16. Dispersion power-law exponent α for fully connected micromodel with fracture and partially connected micromodel with fracture at injection rates of (a) 0.00108 mL/min, (b) 0.005 mL/min, and (c) 0.023148 mL/min.

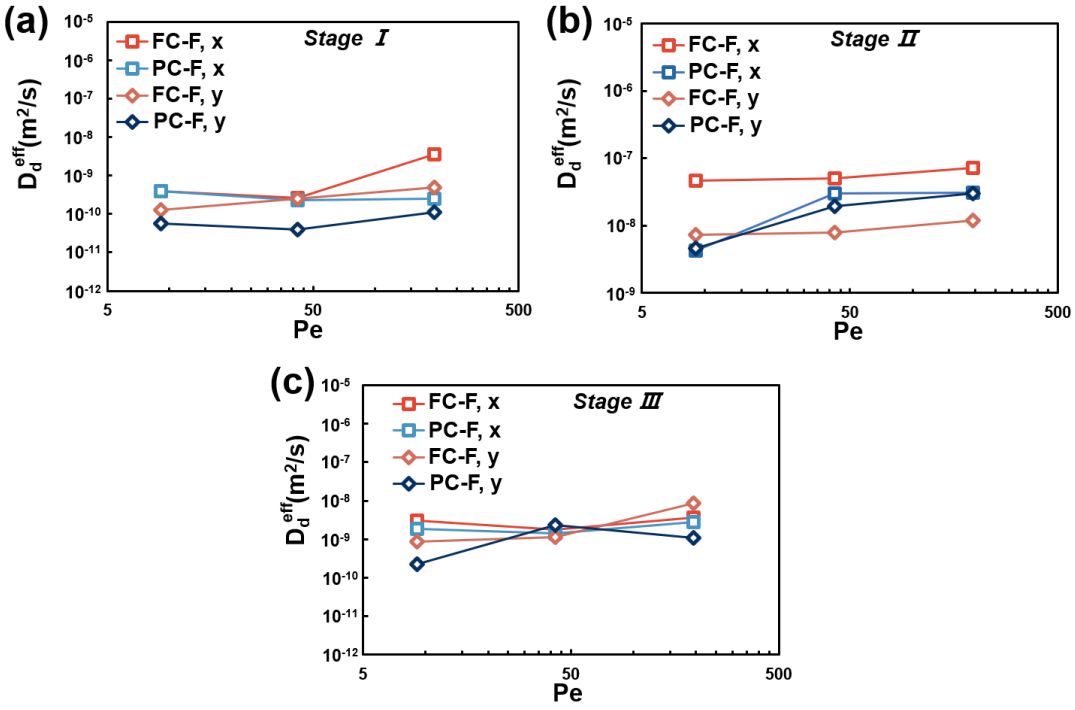

Figure S17. D_d^{eff} versus Pe for Stage I (a), Stage II (b), and Stage III (c) for fully connected micromodel with fracture and partially connected micromodel with fracture.

Table S1 Properties of partially connected micromodel, fully connected micromodel, and core.

	Porosity	Permeability	Average coordination number	Tortuosity
PC micromodel	12.45 %	71.03 mD	3.55	1.76
FC micromodel	13.60 %	300.26 mD	4.58	1.57
Core	12.45 %	73.88 mD	3.51	1.81

Table S2 Spread metrics of the probability density distributions of flow rates for the four micromodels

Micromodel	Weighted Standard Deviation	Interquartile Range	90-10th Percentile Range	95-5th Percentile Range
FC	2.70×10^{6}	2.56×10^{6}	5.37×10^{6}	7.66×10^{6}
PC	1.32×10^{7}	1.22×10^{7}	2.68×10^{7}	3.84×10^{7}
FC-F	7.12×10^{6}	5.55×10^{5}	2.16×10^{6}	3.89×10^{6}
PC-F	8.17×10^{6}	7.25×10^{5}	2.90×10^{6}	5.21×10^{6}

References:

1. J. Liu, K. Duan, Q. Zhang, Y. Zheng, H. Cao and Y. Zhang, *ADV WATER RESOUR*, 2024, **191**, 104780.
2. M. J. Blunt and H. Dong, *PHYS REV E*, 2009, **80**, 36307.
3. L. Song, X. Guo, C. Deng, L. Zhang, Y. Zhang and L. Cao, *Gas Science and Engineering*, 2024, **130**, 205436.
4. H. K., N. E. S., M. N. and K. K. A., *IEEE T IMAGE PROCESS*, 1998, **7**, 1684-1699.
5. Y. Li, X. Chang, W. Yin, G. Wang, J. Zhang, B. Shi, J. Zhang and L. Mao, *MAR PETROL GEOL*, 2019, **102**, 680-694.
6. Y. Makhloufi, P. Collin, F. Bergerat, L. Casteleyn, S. Claes, C. David, B. Menendez, F. Monna, P. Robion, J. Sizun, R. Swennen and C. Rigollet, *MAR PETROL GEOL*, 2013, **48**, 323-340.
7. B. Lecampion, A. Bunger and X. Zhang, *J NAT GAS SCI ENG*, 2018, **49**, 66-83.
8. Z. Li, H. Luo, P. Bhardwaj, B. Wang and M. Delshad, *J PETROL SCI ENG*, 2016, **147**, 395-407.
9. L. Huang, M. Lu, G. Sheng, J. Gong and J. Ruan, *LITHOSPHERE-US*, 2022, **2021**, 4442001.
10. A. Ratanpara, Y. Li and M. Kim, *LAB CHIP*, 2025.
11. K. Ren, J. Zhou and H. Wu, *ACCOUNTS CHEM RES*, 2013, **46**, 2396-2406.
12. D. W. King and D. R. Kester, *MAR CHEM*, 1989, **26**, 5-20.
13. S. Cooper, *Industrial & Engineering Chemistry Analytical Edition*, 1941, **13**, 466-470.
14. H. Y. Birgisson, Y. Xu, M. Moura, E. G. Flekkøy and K. J. Måløy, *ADV WATER RESOUR*, 2025, **198**, 104916.
15. W. L. Marshall and E. U. Franck, *J PHYS CHEM REF DATA*, 1981, **10**, 295-304.
16. H. Arcis, M. Bachet, S. Dickinson, I. Duncanson, R. W. Eaker, J. Jarvis, K. Johnson, C. A. Lee, F. Lord, C. Marks and P. R. Tremaine, *J PHYS CHEM REF DATA*, 2024, **53**, 23103.
17. H. Arcis, J. P. Ferguson, J. S. Cox and P. R. Tremaine, *J PHYS CHEM REF DATA*, 2020, **49**, 33103.
18. A. L. Soli and R. H. Byrne, *MAR CHEM*, 2002, **78**, 65-73.
19. L. N. Plummer and E. Busenberg, *GEOCHIM COSMOCHIM AC*, 1982, **46**, 1011-1040.